





Solutal-buoyancy-driven intertwining and rotation of patterned elastic sheets

Raj Kumar Manna ^a, Oleg E. Shklyaeu ^a, Howard A. Stone ^b and Anna C. Balazs ^{a,*}

^aDepartment of Chemical Engineering, University of Pittsburgh, Pittsburgh, PA 15260, USA

^bDepartment of Mechanical and Aerospace Engineering, Princeton University, Princeton, NJ 08544, USA

*To whom correspondence should be addressed: Email: balazs@pitt.edu

Edited By: Karen E. Nelson.

Abstract

The intertwining of strands into 3D spirals is ubiquitous in biology, enabling functions from information storage to maintenance of cell structure and directed locomotion. In synthetic systems, entwined fibers can provide superior mechanical properties and act as artificial muscle or structural reinforcements. Unlike structures in nature, the entwinement of synthetic materials typically requires application of an external stimulus, such as mechanical actuation, light, or a magnetic field. Herein, we use computational modeling to design microscale sheets that mimic biology by transducing chemical energy into mechanical action, and thereby self-organize and interlink into 3D spirals, which spontaneously rotate. These flexible sheets are immersed in a fluid-filled microchamber that encompasses an immobilized patch of catalysts on the bottom wall. The sheets themselves can be passive or active (coated with catalyst). Catalytic reactions in the solution generate products that occupy different volumes than the reactants. The resulting density variations exert a force on the fluid (solutal buoyancy force) that causes motion, which in turn drives the interlinking and collective swirling of the sheets. The individual sheets do not rotate; rotation only occurs when the sheets are interlinked. This level of autonomous, coordinated 3D structural organization, intertwining, and rotation is unexpected in synthetic materials systems operating without external controls. Using physical arguments, we identify dimensionless ratios that are useful in scaling these ideas to other systems. These findings are valuable for creating materials that act as “machines”, and directing soft matter to undergo self-sustained, multistep assembly that is governed by intrinsic chemical reactions.

Significance Statement:

Through computational modeling, we designed immobile and mobile catalyst-coated surfaces in a fluidic microchamber to orchestrate the spontaneous intertwining of 2D flexible, mobile sheets into a self-rotating 3D spiral. Instead of mechanical, electrical, or optical forces, the process involves inherent chemical reactions on the catalytic patches to convert chemical energy into mechanical action, thereby mimicking chemo-mechanical transduction in biological systems. The findings reveal how specific placements of the catalytic patches within the chamber enable control over the structure–formation and dynamic behavior in the system. The results provide guidelines for regulating the spatiotemporal self-organization of flexible layers into hierarchically structured, dynamic 3D objects without the use of externally applied power.

Introduction

To create synthetic materials that mimic the diversity of movement observed in nature, researchers are designing “active matter,” which consumes chemical energy to undergo motion (1–3). Active matter exhibits one of the hallmarks of living systems: chemo-mechanical transduction, where chemical reactions break down nutrients to fuel mechanical actions (4). Through these research efforts, scientists have fabricated a range of active microparticles that individually, or as a self-organized assembly, achieve biomimetic propulsion, i.e., autonomous movement in a straight line or specified direction (5–7). Rotation constitutes another fundamental component of movement, allowing organisms to change direction in an efficient manner (8, 9). Isolated, active particles can rotate by spinning (10) and assemblies of these particles can form rotating microstructures (11, 12). In most cases,

the larger, rotating object is composed of rotating particles; there are few examples of active, rotating assemblies formed from units that do not spin (13–16). Furthermore, these rotating microstructures are typically 2D objects, like flat rotors (17) or gears (18), and do not assemble into more functional 3D forms. Recently, computational models were developed to examine active matter with greater structural diversity than hard particles; the systems encompassed active, 2D flexible sheets (from the μm to mm size scale) immersed in a fluid-filled chamber (19–21). The sheets and/or chamber walls were coated with catalysts and underwent chemo-mechanical transduction as the catalysts decomposed reactants (“nutrients”) into products and thereby “fueled” the motion of the fluid and flexible sheets. The studies revealed that the sheets spontaneously move and morph into a variety of controllable 3D shapes (22, 23). Herein, we use computational modeling to

Competing Interest: The authors declare no competing interest.

Received: February 24, 2022. **Accepted:** May 24, 2022

© The Author(s) 2022. Published by Oxford University Press on behalf of the National Academy of Sciences. This is an Open Access article distributed under the terms of the Creative Commons Attribution-NonCommercial-NoDerivs licence (<https://creativecommons.org/licenses/by-nc-nd/4.0/>), which permits non-commercial reproduction and distribution of the work, in any medium, provided the original work is not altered or transformed in any way, and that the work is properly cited. For commercial re-use, please contact journals.permissions@oup.com

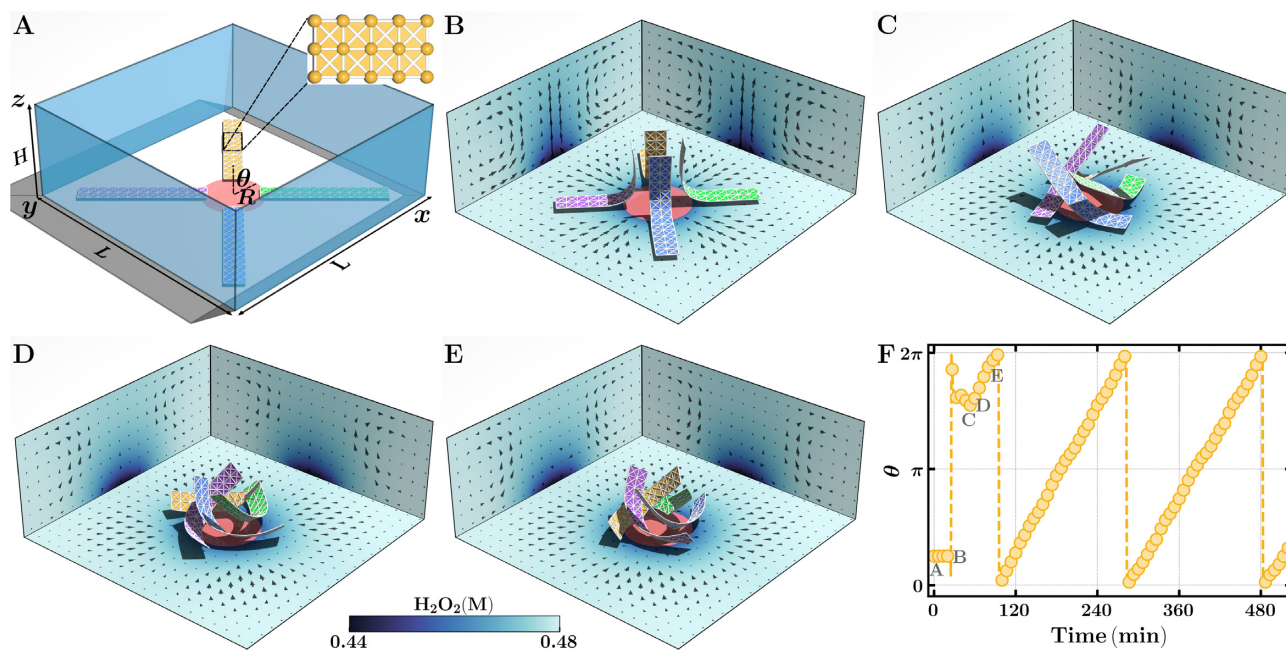


Fig. 1. Dynamic self-assembly and self-rotation of passive sheets. (A) Schematic view of a fluid-filled chamber containing a chemical pump (marked by red circular region of radius R) and four passive elastic sheets (four different colors are guide to the eye). The inset shows the network of nodes (marked by yellow dots) that form the sheet and the flexible bonds between nodes (white lines). (B) and (C) Inward fluid flow generated by the catalytic patch drags sheets toward the center of the chamber to form a tower-like structure (B) that develops into an interlinked assembly (C). (D) and (E) The interlinked configuration rotates in the presence of convective fluid flow (see Movie S1, Supplementary Material). (F) The temporal trajectory of the angle (θ) of the yellow sheet demonstrates the periodic rotation of the assembly. Times for the sheets configurations are marked in (F). Stretching and bending moduli of the sheet are $\kappa_s = 60$ pN and $\kappa_b = 2.25$ pN mm², respectively. The radius and reaction rate of the catalytic patch respectively are $R = 0.5$ mm and $r_m^{\text{patch}} = 90 \mu\text{mol m}^{-2}\text{s}^{-1}$.

design multiple sheets that self-organize into a rotating 3D spiral. Each sheet alone does not rotate, but clustered around a stationary catalytic patch, they rise upward, intertwine with one another, and form a vertical, revolving structure.

The dynamic assembly of the sheets grossly resembles the biological interlinking of strands into a 3D helix, as in the formation of DNA, the assembly of microfilaments, and the coordination of flagella. The spontaneous 3D structural organization, intertwining, and rotation observed here, involving sequential coordinated steps, is not commonly evident in synthetic materials systems. This level of autonomous, self-sustained behavior is invaluable for creating materials systems that act as machines (24), advancing the development of soft robots (25, 26), and more generally, providing insight into directing self-organization in nonequilibrium systems (27–30).

The distinctive collective motion of the immersed sheets is initiated by adding appropriate chemical reactants to a liquid-filled chamber, which encompasses an immobilized catalytic patch on the bottom wall (Fig. 1A). The reactants are catalyzed to generate the reaction products. If these products occupy different volumes than the reactants, then the reaction generates local density gradients, which exert a force on the fluid that propels its motion. (The force that arises from the density gradients is a solutal buoyancy force, as detailed further below.) The flowing fluid in turn drives the sheet upward in a tower-like configuration that experiences an instability. As a result, a new configuration develops where the sheets entwine or “self-link” and undergo the collective swirling shown in Fig. 1(C).

Eventually, all the reactants are consumed in this energy transducing, dissipative system. The solution, however, can be refueled and the entire process can be revived with the addition of new chemicals to the fluid. Such chemically driven self-linking,

self-rotating elastic sheets constitute new modes of dynamic self-assembly and can provide new functionality to microfluidic devices, all without the need for mechanical or electrical pumps. Below, we describe our model for simulating these interconnected dynamic events and detail how various control parameters (e.g., the stiffness and chemical reactivity of the sheets) affect the global behavior of the system.

It is worth noting that experimentalists are beginning to examine the behavior of flexible sheets that are coated with catalytic patches and immersed in fluid-filled microchambers. Recent studies (31) experimentally validated our earlier prediction (20) that sheets coated with enzymes (catalase) can undergo directed motion and shape-changing when the appropriate reactant (hydrogen peroxide) is added to the solution. The researchers note that the observed behavior can be rationalized in terms of the solutal buoyancy mechanism (described below), as we had predicted (32) through our computational modeling of chemically active sheets. Hence, the experiments support our observation that the system undergoes chemo-mechanical transduction, where catalytic reactions drive the mechanical deformation of the immersed active layers (20, 21). The latter agreement between experiments and modeling gives credence to the new predictions detailed below.

Computational Model

The simulation box contains a surface-anchored circular catalytic patch of radius R (Fig. 1A) and mobile elastic sheets in a fluid-filled chamber. In the first instance, we consider sheets that are not coated with catalyst and hence are termed “passive”. We also consider the behavior of active sheets, which are coated with a layer of catalysts. With the addition of the appropriate reactants to the surrounding fluid, the catalysts on the patch decompose the

chemical reactants into products. The products can occupy different volumes than the reactants, leading to local density variations in the fluid, which gives rise to a buoyancy force per unit volume, \mathbf{F}^b , that acts on the fluid. The force is expressed as $\mathbf{F}^b = \mathbf{g}\rho_0 \sum \beta_i C_i$, where ρ_0 is the solvent density, \mathbf{g} is gravitational acceleration, C_i is the concentration of chemical species i , and $\beta_i = \frac{1}{\rho_0} \frac{\partial \rho}{\partial C_i}$ are the corresponding solutal expansion coefficients. This buoyancy force density, \mathbf{F}^b , drives the spontaneous motion of the fluid. In other words, the immobile catalytic patch works as a “chemical pump” that drives the fluid flow via the solutal buoyancy (33, 34) mechanism. Along the bottom surface, if the density of the products is less than the density of the reactants, the flow will move toward the patch and this flow is referred to as “inward” flow. Alternatively, if the products are denser than the reactants, the fluid flow on the bottom surface is away from the patch and is referred to as “outward” flow. Since the fluid is confined in the chamber, it will undergo a circulating motion, as shown in Fig. 1(B).

In the system considered here, the temperature changes due to chemical reaction are assumed small, and thus the effect of thermal buoyancy is neglected (35, 36). We also neglect any enthalpic changes associated with the mixture of the chemicals.

The viscous stresses generated by the fluid flow change the position and shape of the immersed elastic sheet, which is modeled as an initially planar network of nodes, with positions \mathbf{r}_k , that are interconnected by elastic rods (inset of Fig. 1A). The nodes of the sheet experience body forces, $\mathbf{F}^{\text{sheet}} = \mathbf{F}^e + \mathbf{F}^s + \mathbf{F}^g$, which are the respective elastic, steric, and gravity forces. The elastic forces, \mathbf{F}^e , are characterized by the stretching (κ_s) and bending (κ_b) moduli and are governed by the linear constitutive relations for a Kirchhoff rod (37) (see Supplementary Information). The steric forces on the sheet, \mathbf{F}^s , are the sum of the “node–node” (nn) repulsion between two nodes, \mathbf{F}^{nn} , and repulsion between nodes and any of the six confining walls, \mathbf{F}^{nw} . These steric forces are calculated as the gradient of a Morse potential that ensures the equilibrium separation between node–node or node–wall to be r_0 (see Supplementary Information). Gravity acting on the sheet is described by $\mathbf{F}^g = V(\rho_s - \rho_0)\mathbf{g}$, where V is the effective volume of each node and the density of the sheet (ρ_s) is assumed to be greater than the density of the solvent (ρ_0). In the absence of reactants, the sheet sediments to the bottom of the chamber. In the case of passive sheets, the buoyancy forces (and, thus generated fluid flow) in the chamber arise due to density variations generated solely by the surface-anchored chemical pump. Otherwise, the nodes of active sheets are uniformly coated with a catalyst, in which case the buoyancy forces originate from both the sheet and the chamber-coated chemical pump.

The dynamic interactions between the elastic sheet and flowing fluid are described by the respective continuity and Navier–Stokes (in the Boussinesq approximation (38) equations for the dynamics of an incompressible flow, and the equation for the velocity of the nodes of the elastic sheet:

$$\nabla \cdot \mathbf{u} = 0, \quad (1)$$

$$\frac{\partial \mathbf{u}}{\partial t} + (\mathbf{u} \cdot \nabla) \mathbf{u} = -\frac{1}{\rho_0} \nabla p + \nu \nabla^2 \mathbf{u} + \frac{1}{\rho_0} \mathbf{F}, \quad (2)$$

where

$$\mathbf{F} = \underbrace{\mathbf{g} \rho_0 \sum \beta_i C_i}_{\text{solutal buoyancy}} + \underbrace{\frac{1}{V} (\mathbf{F}^e + \sum \mathbf{F}^{nn} + \sum \mathbf{F}^{nw})}_{\text{sheet}} + (\rho_s - \rho_0) \mathbf{g}. \quad (3)$$

$$\frac{\partial \mathbf{r}_k}{\partial t} = \mathbf{u}$$

Here, the body force per unit volume, \mathbf{F} , acting on the fluid arises due to the solutal buoyancy force density and the body force

density exerted by the sheet on the fluid. The immersed boundary method (IBM) (37) is used to treat the fluid–structure interactions. In the IBM, the velocity of each node of the sheet is determined by the fluid velocity at the position of the node (Eq. 3). Also, \mathbf{u} and p are the local fluid velocity and pressure respectively, ν is the kinematic viscosity of the fluid, and ∇ is the spatial gradient operator.

The dynamics of dissolved chemical species C_i in the chamber is governed by an advection–diffusion–reaction equation:

$$\frac{\partial C_i}{\partial t} + (\mathbf{u} \cdot \nabla) C_i = D_i \nabla^2 C_i \pm \underbrace{K_d^{\text{patch}} \sum \delta(\mathbf{r}_{\text{patch}} - \mathbf{r})}_{\text{patch}} \pm \underbrace{K_d^{\text{sheet}} \sum_{k=1}^{N_s} \delta(\mathbf{r}_k - \mathbf{r})}_{\text{sheet}}. \quad (4)$$

Here, D_i is the diffusion constant for the i th reagent of concentration C_i . When the sheets are passive, the chemical is consumed or produced at the location of a chemical pump with a reaction rate r_m^{patch} . For active sheets, chemical reactions occur at the position of the catalytic node \mathbf{r}_k with a reaction rate given by r_m^{sheet} . The catalytic reactions are modeled using Michaelis–Menten reaction rates (39):

$$K_d^{\text{patch}} = \frac{r_m^{\text{patch}} C_i}{K_M + C_i}, \quad K_d^{\text{sheet}} = \frac{r_m^{\text{sheet}} C_i}{K_M + C_i}. \quad (5)$$

K_M (in units of molarity, M) is the Michaelis–Menten constant. r_m^{patch} and r_m^{sheet} are the maximal reaction rates at the chemical pump and active sheets, respectively. The latter reaction rates are given by the products of the reaction rate per molecule of enzyme k_e (in units of s^{-1}) and the areal concentration of enzyme $[E]$ (in units of mol m^{-2}).

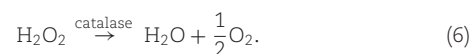
We use no-slip boundary conditions for the fluid flow ($\mathbf{u} = \mathbf{0}$) and no-flux conditions for chemical C_i at the confining walls of the chamber. The numerical methods for solving the governing equations (Eqs. 1–5) with the specific boundary conditions are described in the Methods section. The parameters relevant to chemical reactions are given in Tables S1 and S2 (Supplementary Material).

The dynamic behavior of the elastic sheets depends on a number of physical and chemical variables. In the following section, we first discuss some typical behaviors of the system and then identify dimensionless parameters (see also Supplementary Information) that characterize physical mechanisms regulating the observed phenomena.

Results and Discussion

Self-linking and rotation of passive elastic sheets

We first focus on the dynamic self-assembly and self-rotation of passive elastic sheets in a fluid-filled chamber of lateral dimension $4 \text{ mm} \times 4 \text{ mm}$ and height 1.5 mm . Figure 1(A) shows the four passive sheets placed symmetrically about a centrally located circular patch, which is coated with the enzyme catalase and acts as the chemical pump. All four sheets are identical in size. The length and width of the sheets are respectively 1.95 mm and 0.3 mm and the thickness of the sheets is 0.26 mm . Initially, the sheets are placed parallel to the bottom wall (at height of $1.2r_0$ above the wall) and assume a flat configuration. When hydrogen peroxide (H_2O_2) is added to the chamber, catalase decomposes hydrogen peroxide into less dense products, water (H_2O), and oxygen (O_2) (33,35)



Since the solutal expansion coefficient for oxygen is approximately an order of magnitude smaller than that for the hydrogen peroxide, we neglect its contribution to the density variation in the solution (35). In the systems investigated here, the formation

of O₂ bubbles is also ignored (40) since experiments at comparable conditions showed little or no bubble formation during the catalase-activated decomposition of hydrogen peroxide (40)

Since the product of the reaction is less dense than H₂O₂, the product-rich lighter fluid rises upward and generates inward fluid flow toward the center of the patch along the bottom of the chamber. This inward fluid flow acts on the elastic sheets at the center of the patch and drags them upward, against gravity, to form a 3D tower-like assembly (Fig. 1B and Figure S1, Supplementary Material). The tower can only rise to a particular height until the sheets experience the flow oriented parallel to the top surface (and orthogonal to the vertical line going through the center of the tower). With time, the tower structure becomes unstable and forms an interlinked configuration (see Fig. 1C and Movie S1, Supplementary Material). The dynamics of the interlinking are analogous to the domino effect. Namely, local fluctuations (numerical in the simulation and thermal in the physical system) cause one of the sheets to preferentially bend downward (breaking the symmetry of the system). Due to steric and hydrodynamic interactions, the bending of the first sheet causes its neighbor to bend; the latter sheet drives the bending of the next until all four sheets are interlinked. This interlinking process and the final steady-state configuration result from the fluid–structure interactions, gravity, and steric repulsion between the sheets.

As the first sheet is perturbed sideways, the fluid–structure interactions are no longer completely symmetric and the latter symmetry breaking initiates the motion of the assembly. In the interlinked state, an individual sheet assumes a helical configuration (Fig. 1D and E). Consequently, the convective flow generates a net torque on the sheet and drives the assembly to rotate about the vertical axis that goes through the center of the patch (Fig. 1D and E; the formation of the rotating structure can be visualized by viewing Movie S1.) The angle of rotation (θ), measured between the x-axis and the lateral line connecting the center of the patch and the center of the yellow sheet shows periodic motion over time (Fig. 1F), and thus the assembly has a well-defined angular velocity. This rotating state is stable until the reactant is consumed (corresponding to a few hours in real time, as indicated in Fig. 1F).

Given the initial symmetric placement of the sheets (Fig. 1A), both directions of rotation (clockwise or counterclockwise) are equally probable, and the direction of rotation determines how the sheets are intertwined. The Gauss linking number (41, 42) serves as an order parameter that characterizes the degree of entanglement between two curves. The linking number, Ln , of two 3D curves c_1 and c_2 are defined as

$$Ln(c_1, c_2) = \iint_{c_1 c_2} (d\mathbf{r}_1 \times d\mathbf{r}_2) \cdot \frac{\mathbf{r}_2 - \mathbf{r}_1}{|\mathbf{r}_2 - \mathbf{r}_1|^3}, \quad (7)$$

where \mathbf{r}_1 and \mathbf{r}_2 are the position vectors on the curves c_1 and c_2 , respectively. We use the central line along the long axis of the sheets to compute the linking number (see Supplementary Information for details). Figure 2(A) and (C) shows the linking number between the yellow and green sheets as a function of time for two different initial configurations of the sheets (at a fixed value of the reaction rate at the catalytic patch). In both cases, the sheets are placed symmetrically about the patch, but at different distances from the patch center (Figure S2, Supplementary Material). The assembly begins to rotate when the linking number becomes nonzero. The magnitude of the linking numbers for both cases are the same (since the reaction rate is fixed; see below); however, the sign of the linking number can be either positive or negative. The entwined assembly rotates clockwise for the positive value of

the linking number (Fig. 2B) and counterclockwise for the negative values (Fig. 2C).

The transition from the nearly vertical tower structure of the assembly (Fig. 1B) to the rotating state (Fig. 1D) is marked by a linear instability, as can be seen from Fig. 2(D). In particular, we compute the component of the vorticity of the fluid along the z direction, $\omega_z = (\nabla \times \mathbf{u})_z$ and plot the maximum magnitude of the z-component of the fluid vorticity vector, $|\omega_z|_{\max}$, as a function of time. At time $t = 53.3$ min, $|\omega_z|_{\max}$ displays an exponential increase from its minimum value to the value at the assembly of the rotating state. The exponential evolution is typical of a linear instability in the regime that precedes the formation of the rotating state (43). The magnitudes of the fluid vorticity in the chamber for different times are shown in Figure S3 (Supplementary Material). The plots show that magnitude of the fluid vorticity around the elastic sheets affects the rotational behavior of the assembly.

From the vorticity, we can obtain the angular speed of the rotating assembly and determine parameters that affect the speed. Figure 2(E) reveals a pronounced dependence of the mean angular velocity (Ω ; averaged over five initial configurations) on the reaction rate at the catalytic patch, with Ω increasing with increases in the reaction rate. As the rate of reaction increases, the magnitude of the fluid flow also increases (Figure S4A, Supplementary Material), which leads to an increase in Ω . Thus, the angular speed (or frequency) of the rotating assembly can be tuned by varying the reaction rate of the patch (i.e., by preparing systems with a higher or lower areal concentration of the enzyme).

The state diagram in Fig. 3 further details the influence of the reaction rate on the rotating assembly. We anticipate that the stability of the rotating state is likely to depend on the elasticity of the sheets, reasoning that a stiff sheet would be less sensitive to the flow field than a flexible one. Hence, the state diagram is plotted with the bending modulus of the sheet on the vertical axis and the reaction rate at the patch on the horizontal axis. The diagram indicates regions where the rotating state is stable and where the rotating structure is not formed. To obtain the stable rotating state, the catalytic reaction rate (and thus magnitude of the fluid flow in the chamber) must be above a critical value so that the forces from the fluid flow can morph the sheet to the interlinked configuration (Fig. 3B) for a sustained period of time. The temporal behavior (Fig. 3D) for the configuration in Fig. 3(B) shows that the center of each sheet undergoes regular spatial oscillations in the rotating state. Here, the initial concentration of reactant was chosen so that the sheets' rotational motion is stable for hours, allowing us to carefully focus on this behavior. (As shown in Figure S4B (Supplementary Material), the duration of stable rotation depends on the initial concentration of the reactants.)

For a higher reaction rate ($r_m^{\text{patch}} > 95 \mu\text{mol m}^{-2}\text{s}^{-1}$), the fluid flow is sufficiently large in magnitude that each sheet follows the closest convective rolls generated in the fluid and does not form the stable interlinked configuration (Fig. 3C) that is necessary for the stable rotation of the assembly. In the nonrotating state, the sheets move irregularly within the chamber (Fig. 3E; Figure S5 and Movie S1, Supplementary Material).

The temporal motion of the height of the top of sheets (z_s) in Fig. 3(D) provides additional insight into the dynamics of the rotating assembly and symmetries in the conformations among the different sheets. After a relatively short time, all the curves for z_s versus time exhibit pronounced oscillatory behavior. For a given curve, the transition from the nonoscillatory to oscillatory state reflects the structural transition from the stationary tower to the regularly rotating assembly. Notably, the oscillations

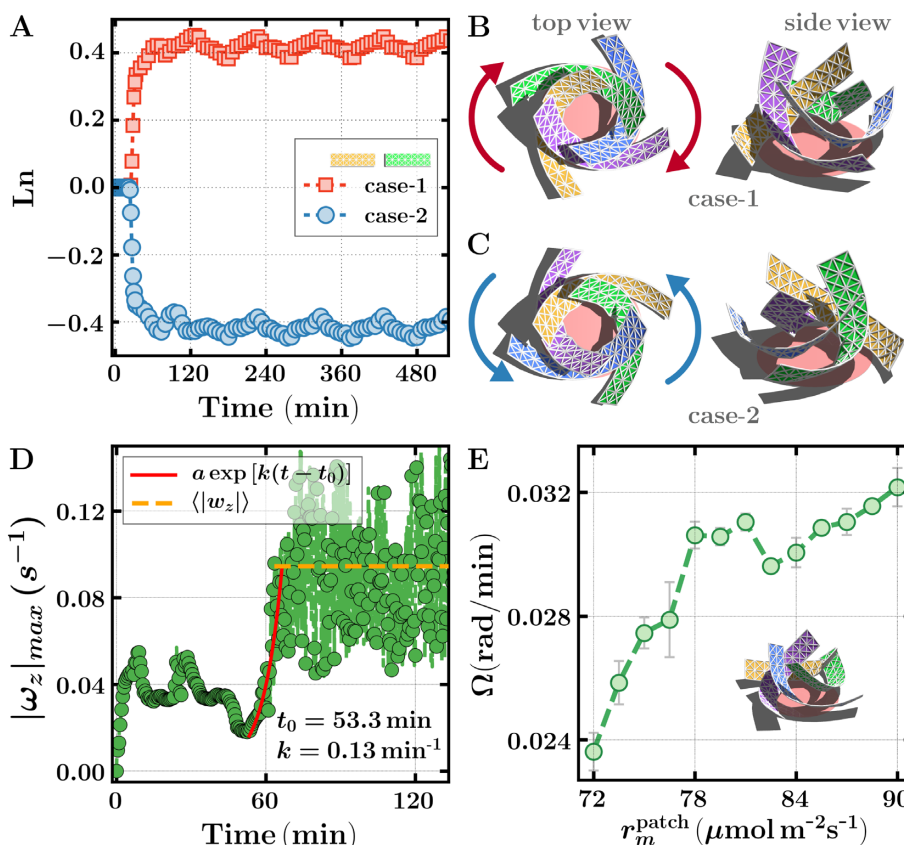


Fig. 2. Direction and angular speed of rotating assembly, and vorticity of the flow. (A) Gauss linking number (Ln) between yellow and green sheets are plotted for two different initial configurations, where the sheets are initially placed symmetrically about the patch, but at different distances from the center of the patch (Figure S2, Supplementary Material). (B) and (C) The direction of rotation depends on the sign of the linking number. For clockwise (B) and counterclockwise (C) rotation, the linking number is positive and negative, respectively. (D) The maximum magnitude of the z-component of vorticity ($|\omega_z|_{max}$) in the chamber as a function of time. The exponential fit (red line) indicates that $|\omega_z|_{max}$ increases exponentially from its minimum value (at $t = 53.3$ min) to a stable value, corresponding to a steady rotating state. (E) The mean angular speed increases with the reaction rate of the patch. The error bar denotes the standard deviation from five initial configurations; inset shows the typical configuration of the rotating assembly. Stretching and bending moduli of the sheets are the same as Fig. 1. The reaction rates of the catalytic patch in (A–D) are the same as Fig. 1.

of the yellow and blue sheets are approximately in phase, as are the oscillations between the green and purple sheets. Furthermore, the oscillations between the respective pairs are approximately out of phase. As seen in Fig. 1(A), the blue and purple sheets lie adjacent to each other, as do the green and yellow. The green sheet lies diagonally across from the purple and the yellow sheet lies diagonally across from blue. Figure 3(F) shows the linking number between different pairs of sheets; Ln assumes two values, one for a pair of adjacent sheets and another for pairs of opposite sheets. Due to their closer proximity, the magnitude of the linking number between adjacent pairs of sheets is greater than that of between opposite pairs. The images in the panels of Fig. 2(B) and (C) allows visualization of the similarity in conformations having the same linking number. Additionally, the oscillations between the yellow and green lines in Fig. 3(F) indicate an out-of-phase difference in the motion of adjacent pairs; similar oscillations between the purple and brown lines indicate an out-of-phase difference in the motion between opposite pairs. These observations reveal the complementary motion between one pair of sheets and another. In addition to the reaction rate at the patch, the height of the sheets in the chamber can be tuned by varying the height of the chamber. Since the velocity of the fluid flow increases with the height of the chamber (H), the height of the sheets also increases with H (Figure S6, Supplementary Material).

To probe the robustness of the interlinked, rotating state, we varied the length of the sheets, considering cases where $l_s = 1.35$ mm, 1.65 mm, and 1.95 mm. (All four sheets in a set are identical in size.) Here, the reaction rate at the patch is fixed to $r_m^{patch} = 78 \mu mol m^{-2} s^{-1}$. The top panels in Fig. 4 demonstrate that the rotating states can be achieved for all three lengths. The configuration of the assembly for the shortest length ($l_s = 1.35$ mm) is different from those for the other two lengths. Consequently, the linking number also depends on the sheet length. For the longer sheets (1.65 mm and 1.95 mm), the linking number between adjacent sheets in an assembly are all identical (Figure S7 and Movie S2, Supplementary Material). In contrast, for the shortest length, the linking numbers between adjacent sheets in the assembly exhibit two distinct values (Figure S7, Supplementary Material). As can be seen in Fig. 4(A)–(C), the short sheets are not sufficiently long to show the same extent of interweaving possible with longer sheets. We do nevertheless observe stable rotation for assemblies with all three lengths (Movie S2, Supplementary Material).

To test the consistency of the observed phenomenon, we varied the widths of sheets, considering $w_s = 0.3$ mm, 0.45 mm, and 0.6 mm. (The widths of all four sheets for a given value of w_s are identical.) The bottom panels in Fig. 4 show the dynamic self-assembly and self-rotation of the sheets for all three widths. Rotating configurations shown in

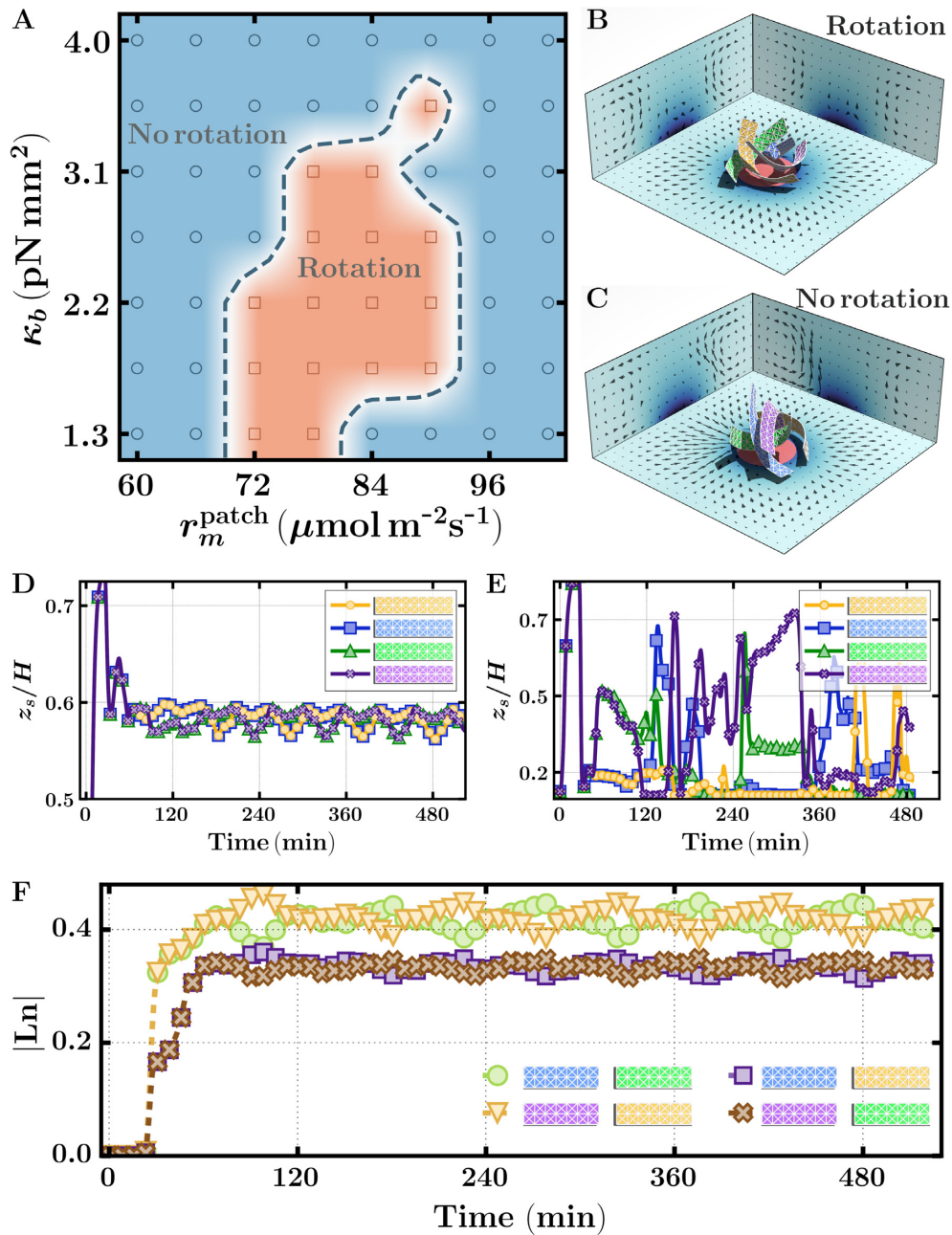


Fig. 3 State diagram of the rotating and nonrotating states of passive elastic sheets. (A) State diagram of passive elastic sheets as a function of bending modulus of the sheets and reaction rate of the catalytic patch. The rotating and nonrotating states are marked by squares and circles, respectively. The colors are guide to the eye. (B) The configuration of the sheets in the rotating state is a stable interlinked structure. (C) The typical configuration in the nonrotating state is an irregular one and changes with time (see Movie S1, Supplementary Material). (D) and (E) The temporal evolution of height of the top of sheets (z_s) are shown for the rotating (D) and nonrotating state. (F) The magnitude of the linking number between adjacent sheets and diagonally opposite sheets are shown as a function of time. Here, the stretching modulus of the sheets is the same as in Fig. 1. The bending modulus of the sheets in (B)–(F) is the same as in Fig. 1. The reaction rates of the catalytic patch in (B), (D), and (F) and in (C) and (E) are respectively $90 \mu\text{mol m}^{-2}\text{s}^{-1}$ and $111 \mu\text{mol m}^{-2}\text{s}^{-1}$.

Fig. 4(D)–(F) are obtained with the same size of the fluid chamber ($6 \text{ mm} \times 6 \text{ mm} \times 2.0 \text{ mm}$) and with the same reaction rate at the patch, $r_m^{\text{patch}} = 66 \mu\text{mol m}^{-2}\text{s}^{-1}$. As the sheet width is increased, the bending deformation of the sheets due to fluid flow becomes less pronounced. Consequently, the magnitude of the linking number that characterizes the degree of intertwining decreases with the increases in w_s (Figure S8, Supplementary Material; to obtain self-rotation with an even wider sheet, we would need to increase the size of the fluid chamber so that the bottom surface can accommodate four sheets without overlapping.)

The interlinking and rotating of the sheets are sufficiently consistent that it is observed with eight passive sheets in the chamber, for two different reaction rates (Figure S9 and Movie S3, Supplementary Material). At each reaction rate, the sheets self-assemble into distinct interlinked configurations that spontaneously undergo rotation. The self-rotation can also be achieved for different shapes and sizes of catalytic patches. Figure S10 (Supplementary Material) shows the self-rotation of four passive sheets with a square catalytic patch. Since the area of the square catalytic region is different than the circular patch, we tuned the reaction

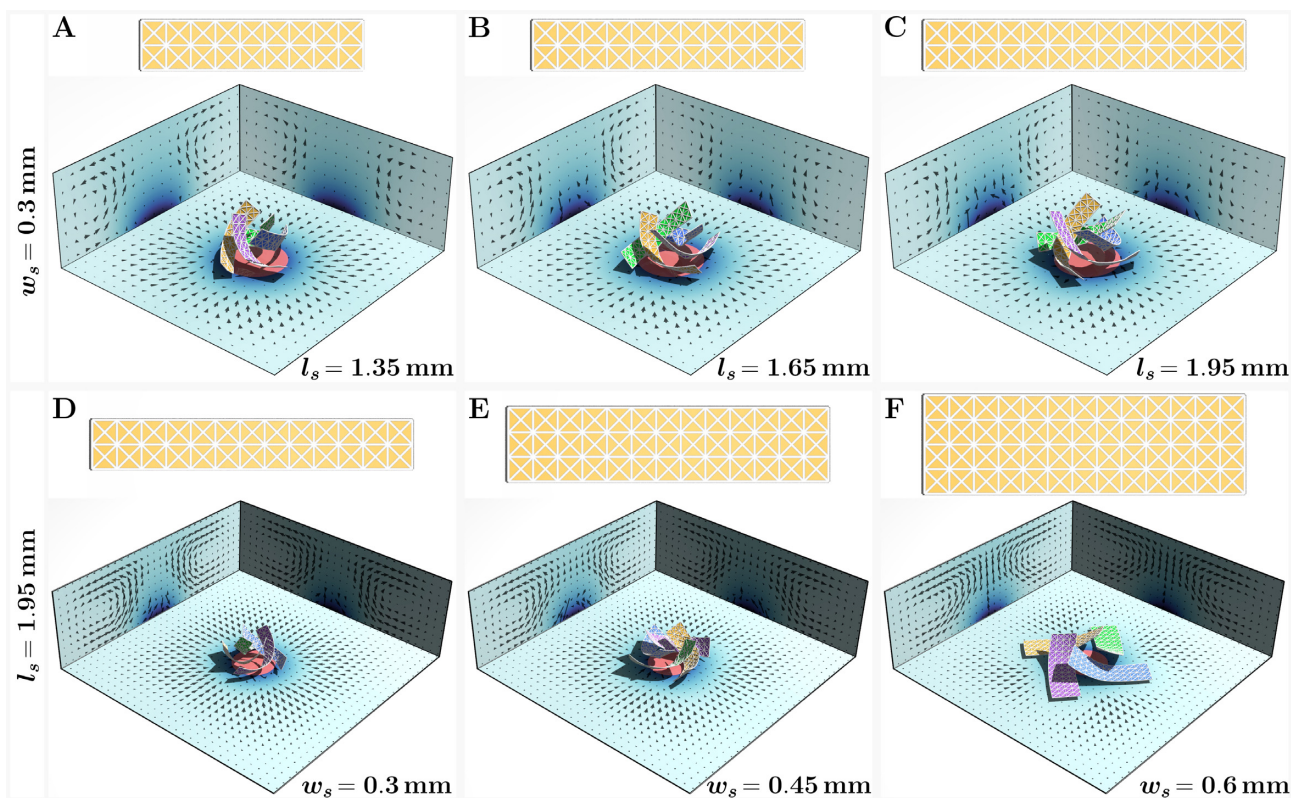


Fig. 4. Self-rotation of passive sheets of different lengths and widths. (A)–(C) The configuration of the rotating state of the passive sheets of lengths 1.35 mm, 1.65 mm, and 1.95 mm are respectively shown in A, B, and C. The width of the sheet is 0.3 mm and the reaction rate of the patch is $r_m^{\text{patch}} = 78 \mu\text{mol m}^{-2}\text{s}^{-1}$. The snapshots in (A)–(C) are at 108 min after the start of the chemical reaction. (D) and (E) The typical snapshot of the rotating state of passive sheets of widths 0.3 mm, 0.45 mm, and 0.6 mm are shown in D, E, and F, respectively. The length of the sheet is 1.95 mm and the reaction rate of the patch is $r_m^{\text{patch}} = 66 \mu\text{mol m}^{-2}\text{s}^{-1}$. The configurations of the assembly are at 167 min. The sizes of the fluid chamber in (A)–(C) and (D) and (E) are $4 \text{ mm} \times 4 \text{ mm} \times 1.5 \text{ mm}$ and $6 \text{ mm} \times 6 \text{ mm} \times 2.0 \text{ mm}$, respectively. Stretching and bending moduli of the sheet are $\kappa_s = 60 \text{ pN}$ and $\kappa_b = 2.25 \text{ pN mm}^2$, respectively.

rate of the patch to obtain the self-rotating state. Furthermore, the assembly and rotating behavior of the elastic sheets can be altered by introducing a ring-shaped catalytic patch (Figure S11, Supplementary Material). This collection of simulations indicates that self-rotating behavior is robust and can be achieved with the appropriate choice of reaction rate or elasticity of the sheets.

Self-rotation of chemically active sheets

The dynamic assembly and rotation of the sheets are altered when the sheets are active, i.e., coated with catalysts. The rotating state of four catalase-coated elastic sheets is shown in Fig. 5A (see Movie S3, Supplementary Material). Now, the fluid flow in the chamber is generated by catalytic reactions on both the patch and sheets. Hence, for a fixed bending and stretching moduli, the state diagram (Fig. 5B) of active sheets can be controlled by varying reaction rate of the patch (r_m^{patch}), as well as reaction rate of the sheets (r_m^{sheet}). Since catalase-coated sheets also generate flow in the chamber, the r_m^{patch} necessary to obtain the rotating state of the assembly decreases with an increase of the reaction rate of the sheet r_m^{sheet} . Similarly, r_m^{patch} required for the transition from rotating state to nonrotating states (at which sheets follow convective rolls and move irregularly) decreases with the increase of r_m^{sheet} . For higher reaction rates at the sheets ($r_m^{\text{sheet}} > 15 \mu\text{mol m}^{-2}\text{s}^{-1}$), the fluid flow in the chamber is sufficiently large in magnitude that active sheets do not form stable rotating structures for all values of the patch reaction rates considered here.

Unlike the case for passive sheets where clockwise or counterclockwise rotation is equally probable and cannot be controlled a priori, the directionality of the rotation can be achieved by just partially coating the sheets. Examples of this behavior are shown in Fig. 5(C)–(F) and Movie S4 (Supplementary Material). The initial arrangement of the partially coated sheets in Fig. 5(C) (and in Fig. 5E) breaks the rotational symmetry due to the patterning of the sheets and subsequent asymmetry in the fluid flow (with respect to the long axis of the sheet). Thus, the generated fluid flow for the case in Fig. 5(C) always drives the sheets to assemble into a right-handed helical structure (Fig. 5D), while the case in Fig. 5(E) always yields the left-handed helical structure (Fig. 5F). Hence, sheets always rotate in clockwise for the case in Fig. 5(C) and counterclockwise for the case in Fig. 5(E).

Influence of different variables on the swirling of the passive sheets

Recall that the dynamics of the passive elastic sheets depends on a number of variables, such as reaction rate (r_m^{patch}) and radius (R) of the catalytic patch; initial concentration (C_{10}) and diffusivity (D) of the chemical; and density (ρ_s) and elastic properties (κ_s and κ_b) of the sheet. We consider the size of the chamber and the sheets to be fixed. By analyzing the effects of the individual variables, we establish a dimensionless parameter that governs the dynamics of the sheets. To facilitate this analysis, we characterize the movement and reconfiguration of a sheet from its initial flat state

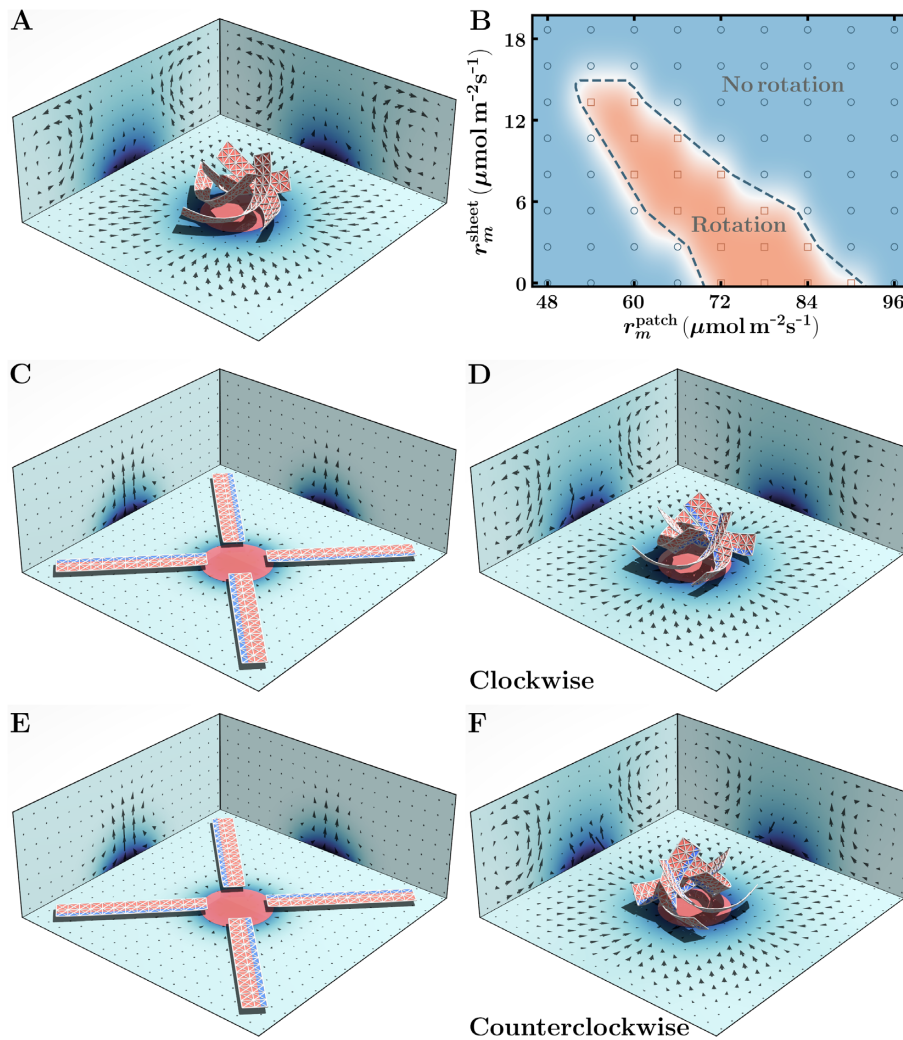


Fig. 5. Self-rotation of chemically active sheets. (A) Fluid flow generated by four catalase-coated elastic sheets and the chemical pump drives the elastic sheets into an interlinked configuration that spontaneously rotate. The reaction rate of the patch and sheets are respectively $r_m^{\text{patch}} = 78 \mu\text{mol m}^{-2}\text{s}^{-1}$ and $r_m^{\text{sheet}} = 6.67 \mu\text{mol m}^{-2}\text{s}^{-1}$. (B) State diagram of the chemically active sheets as a function of the catalytic reaction rate of the patch, r_m^{patch} and catalytic reaction rate of the sheets, r_m^{sheet} . Circle and square symbols represent the nonrotating and rotating state of the assembly. (C)–(F) Partially coated sheets are used to achieve stable rotation in a particular direction. The initial positions of the partially coated sheets in (C) and (E) always exhibit clockwise (D) and counterclockwise (F) rotation. The reaction rate of the patch and sheets in (C)–(F) are respectively $r_m^{\text{patch}} = 78 \mu\text{mol m}^{-2}\text{s}^{-1}$ and $r_m^{\text{sheet}} = 2.67 \mu\text{mol m}^{-2}\text{s}^{-1}$. Here, stretching and bending moduli of the sheets are the same as Fig. 1.

through the order parameter, z_m , which is the maximum height of the sheet over time (see Figure S1, Supplementary Material).

We examine the effect of the area of the catalytic patch on the sheet dynamics by varying the radius of the circular patch, R (while keeping all other parameters fixed). For a given reaction rate at the patch (r_m^{patch}), an increase in R enables the patch to catalyze more hydrogen peroxide, leading to an increase in the magnitude of the fluid flow. The increased fluid flow lifts the sheets higher, resulting in higher values of z_m for larger R (Fig. 6A). Consequently, the magnitude of the fluid flow and the dynamics of the sheets is regulated by the parameter $r_m^{\text{patch}} R^2$ (Figure S12A, Supplementary Material).

Since an increase in C_{10} effectively increases the chemical decomposition by a factor of $C_{10}/(K_M + C_{10})$, the parameter z_m increases with an increase of C_{10} for a constant r_m^{patch} (Fig. 6B). Therefore, the parameter $r_m^{\text{patch}} C_{10}/(K_M + C_{10})$ also plays a key role in regulating the dynamics of the sheets (Figure S12B, Supplementary Material).

In addition to initial concentration, the diffusivity of the chemicals contributes in developing the solutal buoyancy force, and hence the strength of the fluid flow. A more rapidly diffusing chemical creates a lower chemical gradient (and lower solutal buoyancy force) in the chamber. Therefore, the magnitude of the fluid flow is lower with higher diffusivity and z_m decreases with an increase of D for a constant r_m^{patch} (Fig. 6C). If the x -axis (r_m^{patch}) is rescaled with the parameter r_m^{patch}/D , then the order parameter z_m for different diffusivities collapse into one curve (Figure S12C, Supplementary Material).

While the physical parameters characterizing the catalytic patch (r_m^{patch} , R) and the chemicals (C_0 , D) determine the strength of the fluid flow, which affects the upward motion of the sheets, gravity acting on the sheets (which is proportional to the density of the sheets) counteracts this upward motion. Figure 6(D) shows that the maximum height of the sheets, z_m , decreases with an increase in the density of the sheets (for a fixed r_m^{patch}). Therefore, when the x -axis is rescaled to $r_m^{\text{patch}}/(\rho_s - \rho_0)$, curves involving dif-

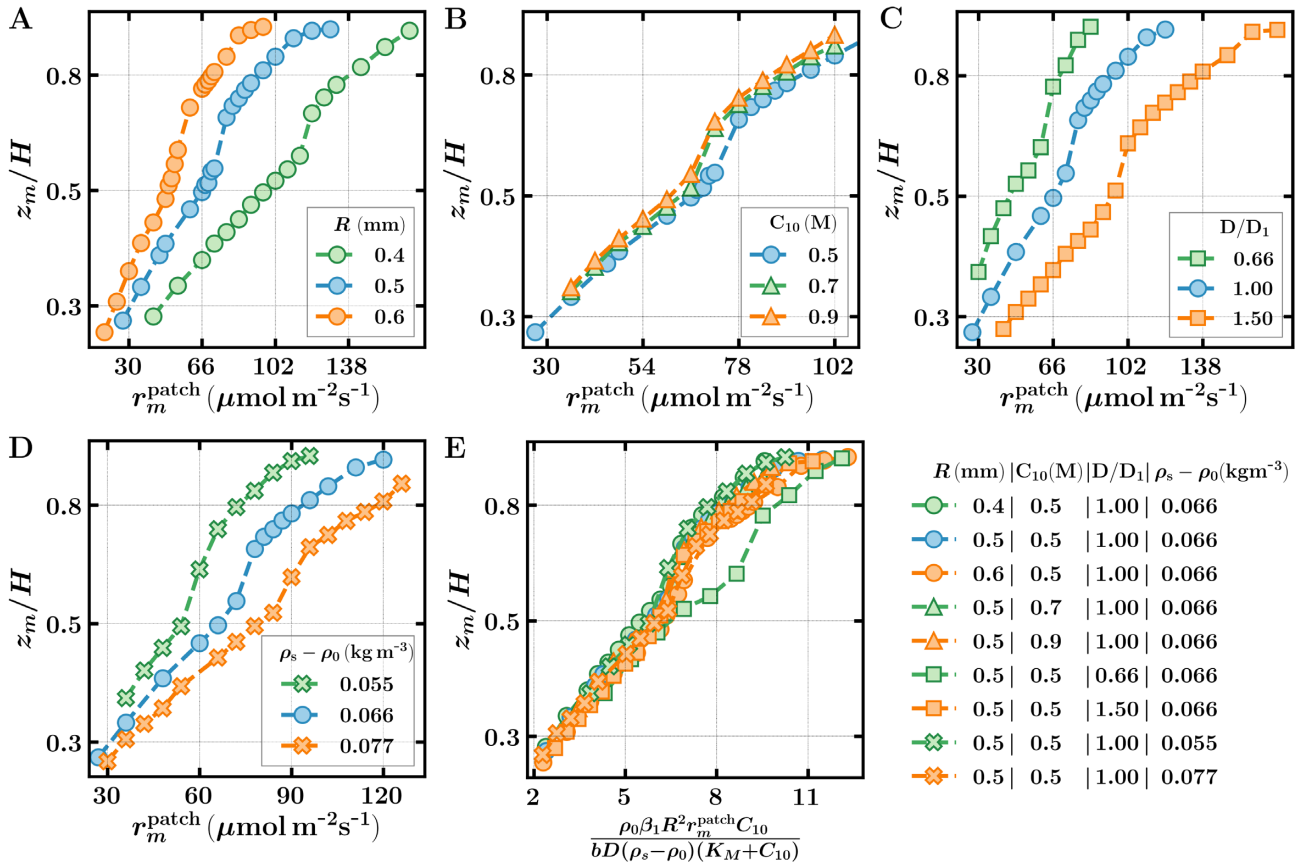


Fig. 6. Quantifying the effect of various physical parameters. (A) The maximum height of the sheet (z_m), scaled with the height of the chamber as a function of catalytic reaction rate of the patch, r_m^{patch} for different radius of the patch, R . All other parameters are kept constant (marked in the inset of E). (B)–(D) The scaled order parameter (z_m/H) as a function of r_m^{patch} for different initial concentration of the chemical (C_{10}), the diffusivity of the chemical (D), and the density of the sheets (ρ_s) are plotted in (B), (C), and (D), respectively. $D = D_1$ is the diffusivity of the hydrogen peroxide. (E) When the x-axis is rescaled to the dimensionless parameter, \tilde{A} (Eq. 7) all the curves in (A)–(D) roughly collapse into one single curve. Here, stretching and bending moduli of the sheets are $\kappa_s = 60$ pN and $\kappa_b = 2.25$ pN mm², respectively.

ferent sheet densities collapse onto a single curve (Figure S12D, Supplementary Material).

The above observations reveal that the dynamics of elastic sheets (of the constant elastic modulus) effectively depend on two competing forces: the solutal buoyancy force and the gravitational force. The ratio of these two forces yields a dimensionless parameter that governs the dynamics of the sheets (see Supplementary Information for details)

$$\tilde{A} = \frac{\rho_0 \beta_1 R^2 r_m^{\text{patch}} C_{10}}{b D_1 (\rho_s - \rho_0) (K_M + C_{10})}, \quad (7)$$

where b is the thickness of the sheet. If the order parameter for various control parameters is plotted with respect to dimensionless parameter, \tilde{A} , then all the data roughly collapse into one master curve (Fig. 6E). The resulting master curve quantifies the effect of the different control parameters and provides insight into the competing forces acting on in the system. Namely, to obtain the upward motion of the sheets, the viscous stresses generated by the fluid flow must be greater than the gravitational force acting on the sheets.

The generated viscous stresses also compete with elastic forces associated with the bending of the sheets. The corresponding dimensionless ratio for a sheet with flexural rigidity B is given by (see Supplementary Information)

$$\tilde{B} = \frac{B D_1 (K_M + C_{10})}{l_s^2 \omega_s \rho_0 \beta_1 R^2 r_m^{\text{patch}} C_{10}}. \quad (8)$$

The typical values of the dimensionless parameters corresponding to the simulation of Fig. 1 are $\tilde{A} = 8$ and $\tilde{B} = 0.0002$.

Discussion

In summary, we demonstrated the spontaneous self-organization of millimeter-sized elastic sheets into interlinked, helical structures that undergo autonomous rotation. This distinctive behavior is due to the solutal buoyancy mechanism, where catalytic reactions on the bottom of the chamber (and on active sheets) generated density variations in the solution. The density variations produced a solutal buoyancy force that drove the fluid flows, which exerted forces on the flexible sheets. The sheets in turn exerted a force on the fluid. This dynamic feedback and the placement of the sheets around a central catalytic pump gave rise to the self-organization and rotation of the spiral assembly. The entire process involved biomimetic chemo-mechanical transduction as the chemical energy released from the reaction was converted into mechanical motion.

The interlinking of the sheets into 3D spiral structures can also be viewed as biomimetic, since the 3D spiral resembles a common motif in nature, from the assembly of DNA to the coordinated movement of cilia and flagella. Notably, the isolated sheets do not undergo rotational motion; rotation was observed only when the sheets were interlinked. The latter property is distinct from the typical behavior for synthetic self-organized microrotors, where

the individual components typically spin and have intrinsic angular momentum (44, 45). In contrast, the individual flexible sheets in our system do not generate torque.

The rotational motion of the interlinked sheets was sensitive to several variables. To determine the role of these different variables, we established the ratio of parameters and identified dimensionless numbers that characterize the system's behavior. Expressed in terms of these dimensionless numbers, we can relate the numbers used in our simulations to the relevant range of physical values and thereby guide future experimental studies. For example, the magnitude of the flow velocities is characterized by the ratio of the solutal buoyancy to viscous forces, expressed as a dimensionless Grashof number, $Gr = g\beta_1 cL^3/\nu^2$, where β_1 is the coefficient of solutal expansion, and c is the characteristic chemical variation across the domain. In our studies, the assembly and rotation of the structures were observed for Grashof number $\sim 2.6 \times 10^2$. Alternatively, the flow can be characterized by the Reynolds number, $Re = uR/\nu$, and Peclet number $Pe = uR/D_1$, where $R = 0.5$ mm is the radius of the catalytic patch, and $u = 33$ $\mu\text{m/s}$ is typical fluid velocity in the chamber. In our simulations, the typical Reynolds number and Peclet number are respectively 0.016 and 11.5.

The elastic properties of the sheet are characterized by the dimensionless flexural rigidity, \tilde{B} (Eq. 8), which is the ratio of the bending stress to the viscous stress. The typical dimensionless flexural rigidity of the sheet considered in this study is ~ 0.0002 . There in fact exist both synthetic and biological thin films that exhibit a flexural rigidity comparable to sheets in our model and, therefore, these materials could enable experimental realization of the assembly. For example, ultrathin flexible sheets of functionalized nanoparticles (NPs) (46, 47), photo-crosslinkable polymer films (48, 49), and sheets composed of oleosin surfactant proteins (50) can be utilized to form chemically active sheets by incorporating catalysts (49, 51) into these films.

The relative importance of the solutal buoyancy force relative to the density of the sheets is characterized by the dimensionless parameter \tilde{A} (Eq. 7). The typical range of dimensionless parameters \tilde{A} used in our simulations was $\sim 2 - 12$.

Finally, this self-rotating system does not require any external input of electrical or mechanical energy. It can be instigated by adding a chemical reactant to the solution; once the reactant is consumed, the rotary motion can be maintained by adding more reactant. Hence, the design concepts presented here can be useful in creating soft robotic structures that display self-sustained action or motion (52). The self-linking, self-oscillatory systems presented here provide guidance for developing autonomous soft robots (53) that operate in solution and can work without any external source of energy. Additionally, the self-assembly of elastic sheets into 3D complex structures by chemically generated fluid flow provides new modes of dynamic self-organization.

Methods

The continuity and Navier–Stokes equations (Eqs. 1 and 2) are solved using the lattice Boltzmann method (LBM) with a single relaxation-time D3Q19 scheme (54). A finite difference approach with a forward-time central-space (FTCS) scheme is used to solve the equation for advection, diffusion, and reaction of the chemicals (Eq. 4). The boundary condition for the fluid flow at the confining walls of the chamber satisfies the no-slip boundary condition ($\mathbf{u} = \mathbf{0}$). For the concentration of chemical C_i , we use two different boundary conditions: (i) no chemical penetration through the walls, $\frac{\partial C_i}{\partial \hat{n}} = 0$, and (ii) the walls are coated with enzyme and take

part in the catalytic reactions, $-D_i \frac{\partial C_i}{\partial \hat{n}} = \frac{r_{\text{patch}} C_i}{K_M + C_i}$. Here, \hat{n} is surface normal pointing into the fluid domain.

The immersed boundary (IB) approach is used to capture the fluid–structure interactions between the elastic sheet and fluid (37, 55). Each node of the elastic sheet is represented by a sphere with effective hydrodynamic radius a that accounts for a fluid drag characterized by the mobility $M = (6\pi\mu a)^{-1}$, where $\mu = \nu\rho_0$ is the dynamic viscosity of the fluid. The forces exerted by the nodes of the elastic sheet on the fluid, calculated using the IB method, provide zero fluid velocities at the discretized nodes of the elastic sheet. Therefore, the IB approach approximates no-slip conditions for the fluid velocities at the nodes. The separation between the nodes of the sheet is sufficiently small that there is no fluid permeation through the nodes constituting the sheet. Since the elastic sheet in our model is composed of one layer of the nodes, the effective thickness of the elastic sheet (b) is equal to the diameter $2a$ of a single node. We keep the thickness of the sheet constant and vary the elastic moduli to alter the mechanical properties of the sheet.

The velocity field $\mathbf{u}(u_x, u_y, u_z)$ computed using the LBM method at each time step of the simulation is used to advect the chemical concentration (Eq. 4) and to update the position of nodes of the elastic sheet (Eq. 3). The updated concentration field is then used to determine the buoyancy forces in Eq. 2. The time step size, Δt , in the simulation is 1.67×10^{-3} s. The sizes of the computational domain are $42\Delta x \times 42\Delta x \times 17\Delta x$ and $62\Delta x \times 62\Delta x \times 22\Delta x$, where the lattice Boltzmann unit Δx is 100 m . The physical dimension of the simulation box corresponding to each figure is given in Table S4 (Supplementary Material). The hydrodynamic radius of the node, a is taken as $1.3\Delta x$. In the discretization of the elastic sheet, the distance between two nearest neighboring nodes is set to $1.5\Delta x$. The dimensions of the elastic sheets and catalytic patch are given in Tables S3 and S4 (Supplementary Material).

Supplementary Material

Supplementary material is available at [PNAS Nexus](#) online.

Funding

We gratefully acknowledge funding from the Department of Energy under grant DE-FG02-90ER45438, the Department of Defense, Army Research Office under grant W911NF-17-1-0351, and the computational facilities at the Center for Research Computing at the University of Pittsburgh.

Authors' Contributions

All authors designed the system described here and determined the studies to be performed. R.K.M. and O.E.S. performed the simulations and numerical calculations. All the authors helped analyze the data and contributed to writing the manuscript.

Data Availability

All data is included in the manuscript and/or supporting information.

References

- Zhang Y., Hess H. 2021. Chemically-powered swimming and diffusion in the microscopic world. *Nat Rev Chem.* 5:500–510

2. Sanchez S., Soler L., Katuri J. 2015. Chemically powered micro- and nanomotors. *Angew Chem Int Ed.* 54:1414–1444
3. Wang J, et al. 2021. Rotational locomotion of an active gel driven by internal chemical signals. *J Phys Chem Lett.* 12:11987–11991 10.1021/acs.jpcclett.1c03128
4. Golestanian R.. 2010. Synthetic mechanochemical molecular swimmer. *Phys Rev Lett.* 105:1–4
5. Bechinger C, et al. 2016. Active particles in complex and crowded environments. *Rev Mod Phys.* 88:045006
6. Ebbens S. J., Howse J. R.. 2010. In pursuit of propulsion at the nanoscale. *Soft Matter.* 6:726
7. Wang W, Duan W, Ahmed S, Mallouk T. E., Sen A.. 2013. Small power: autonomous nano- and micromotors propelled by self-generated gradients. *Nano Today.* 8:531–554
8. Cortese D, Wan K. Y. 2021. Control of helical navigation by three-dimensional flagellar beating. *Phys Rev Lett.* 126:88003
9. Drescher K., et al.. 2009 Dancing volvox: hydrodynamic bound states of swimming algae. *Phys Rev Lett.* 102:1–4
10. Brooks A. M., et al.. 2019 Shape-directed rotation of homogeneous micromotors via catalytic self-electrophoresis. *Nat Commun.* 10:1–9
11. Petroff A. P., Wu X., Libchaber A. 2015. Fast-moving bacteria self-organize into active two-dimensional crystals of rotating cells. *Phys Rev Lett.* 158102:1–6
12. Singh R., Adhikari R. 2016. Universal hydrodynamic mechanisms for crystallization in active colloidal suspensions. *Phys Rev Lett.* 117:1–5
13. Pandey A., Kumar P.B.S., Adhikari R. 2014. Flow-induced nonequilibrium self-assembly in suspensions of stiff, apolar, active filaments. *Soft Matter.* 12:1–5
14. Davies Wykes M. S, et al. 2016. Dynamic self-assembly of microscale rotors and swimmers. *Soft Matter.* 12:4584–4589
15. Aubret A., Youssef M., Sacanna S., Palacci J. 2018. Targeted assembly and synchronization of self-spinning microgears. *Nat Phys.* 14:1114–1118
16. Dreyfus R., Baudry J., Stone H. A. 2005. Purcell's 'rotator': mechanical rotation at low Reynolds number. *Eur Phys J B.* 47:161–164
17. Kim H, et al. 2021. Coupled oscillation and spinning of photothermal particles in Marangoni optical traps. *Proc Natl Acad Sci USA.* 118:e2024581118.
18. Pena-Francesch A., Giltinan J., Sitti M.. 2019. Multifunctional and biodegradable self-propelled protein motors. *Nat Commun.* 10:1–10
19. Manna R. K., Laskar A., Shklyaev O. E., Balazs A. C.. 2021. Harnessing the power of chemically active sheets in solution. *Nat Rev Phys.* 4:1–13.
20. Laskar A., Shklyaev O. E., Balazs A. C.. 2018. Designing self-propelled, chemically active sheets : wrappers, flappers, and creepers. *Sci Adv.* 4:1–12
21. Manna R. K., Shklyaev O. E., Balazs A. C. 2021. Chemical pumps and flexible sheets spontaneously form self-regulating oscillators in solution. *Proc Natl Acad Sci.* 118:e2022987118
22. Manna R. K., Shklyaev O. E., Stone H. A., Balazs A. C.. 2020. Chemically controlled shape-morphing of elastic sheets. *Mater Horiz.* 7:2314–2327
23. Laskar A., Shklyaev O. E., Balazs A. C.. 2021. Self-morphing, chemically driven gears and machines. *Matter.* 4:600–617
24. McCracken J. M., Donovan B. R., White T. J.. 2020. Materials as machines. *Adv Mater.* 32:1906564.
25. Soto F, et al. 2021. Smart materials for microrobots. *Chem Rev.* 122:5365–5403, 10.1021/acs.chemrev.0c00999
26. Kim H, et al. 2020. Shape morphing smart 3D actuator materials for micro soft robot. *Mater Today.* 41:243–269
27. Uchida N., Golestanian R. 2010. Synchronization and collective dynamics in a carpet of microfluidic rotors. *Phys Rev Lett.* 104:1–4
28. Yeo K., Lushi E., Vlahovska P. M. 2015. Collective dynamics in a binary mixture of hydrodynamically coupled microrotors. *Phys Rev Lett.* 114:1–5
29. Nguyen N. H. P., Klotsa D., Engel M., Glotzer S. C. 2014. Emergent collective phenomena in a mixture of hard shapes through active rotation. *Phys Rev Lett.* 112:1–5
30. Grzybowski B. A., Fitzner K., Paczesny J., Granick S. 2017. From dynamic self-assembly to networked chemical systems. *Chem Soc Rev.* 46:5647–5678
31. Mathesh M., Bhattarai E., Yang W. 2022. 2D active nanobots based on soft nanoarchitectonics powered by an ultralow fuel concentration. *Angew Chemie Int Ed.* 61:1–6
32. Ortiz-Rivera I., Shum H., Agrawal A., Sen A., Balazs A. C. 2016. Convective flow reversal in self-powered enzyme micropumps. *Proc Natl Acad Sci.* 113:2585–2590
33. Sengupta S, et al. 2014. Self-powered enzyme micropumps. *Nat Chem.* 6:415–422
34. Shklyaev O. E., Shum H., Sen A., Balazs A. C. 2016. Harnessing surface-bound enzymatic reactions to organize microcapsules in solution. *Sci Adv.* 2:e1501835
35. Das S, et al. 2017. Harnessing catalytic pumps for directional delivery of microparticles in microchambers. *Nat Commun.* 8:1–10
36. Valdez L., Shum H., Ortiz-Rivera I., Balazs A. C., Sen A.. 2017. Solu-tal and thermal buoyancy effects in self-powered phosphatase micropumps. *Soft Matter.* 13:2800–2807
37. Lim S., Ferent A., Wang X. S., Peskin C. S. 2008. Dynamics of a closed rod with twist and bend in fluid. *SIAM J Sci Comput.* 31:273–302
38. Chandrasekhar S.. 1981. Hydrodynamic and hydromagnetic stability. New York (NY): Dover.
39. Johnson K. A., Goody R. S. 2011. The original Michaelis constant: translation of the 1913 Michaelis-Menten paper. *Biochemistry.* 50:8264–8269
40. Maiti S., Shklyaev O. E., Balazs A. C., Sen A.. 2019. Self-organization of fluids in a multi-enzymatic pump system. *Langmuir.* 35:3724–3732
41. Ricca R. L., Nipoti B. 2011. Gauss' linking number revisited. *J Knot Theory Ramificat.* 20:1325–1343
42. Klenin K., Langowski J.. 2000. Computation of writhe in modeling of supercoiled DNA. *Biopolymers.* 54:307–317
43. Strogatz S. H.. 2018. Nonlinear dynamics and chaos: with applications to physics, biology, chemistry, and engineering. Boca Raton (FL): CRC Press.
44. Fily Y., Baskaran A., Marchetti M. C.. 2012. Cooperative self-propulsion of active and passive rotors. *Soft Matter.* 8:3002–3009
45. Leoni M., Liverpool T. B. 2010. Dynamics and interactions of active rotors. *Europhys Lett.* 92:64004
46. Lin Y, et al. 2003. Ultrathin cross-linked nanoparticle membranes. *J Am Chem Soc.* 125:12690–12691
47. Lee D. Y, et al.. 2013. Macroscopic nanoparticle ribbons and fabrics. *Adv Mater.* 25:1248–1253
48. Kim J., Hanna J. A., Byun M., Santangelo C. D., Hayward R. C.. 2012. Designing responsive buckled surfaces by Halftone gel lithography. *Science.* 335:1201–1205
49. Na J.-H. H, et al. 2015. Programming reversibly self-folding origami with micropatterned photo-crosslinkable polymer tri-layers. *Adv Mater.* 27:79–85

50. Vargo K. B., Parthasarathy R., Hammer D. A. 2012. Self-assembly of tunable protein suprastructures from recombinant oleosin. *Proc Natl Acad Sci.* 109:11657–11662
51. Huang Y., Ren J., Qu X.. 2019. Nanozymes: classification, catalytic mechanisms, activity regulation, and applications. *Chem Rev.* 119:4357–4412
52. Grzybowski B. A., Sobolev Y. I., Cybulski O., Mikulak-klucznik B. 2022. Materials, assemblies and reaction systems under rotation. *Nat Rev Mater.* 7:338–354
53. Wehner M, et al. 2016. An integrated design and fabrication strategy for entirely soft, autonomous robots. *Nature.* 536: 451–455
54. Guo Z., Zheng C., Shi B. 2002. Discrete lattice effects on the forcing term in the lattice Boltzmann method. *Phys Rev E Stat Phys Plasmas Fluids Relat Interdiscip Top.* 65:6
55. Shum H., Tripathi A., Yeomans J. M., Balazs A. C. 2013. Active ciliated surfaces expel model swimmers. *Langmuir.* 29:12770–12776. Edited By:Karen E. Nelson.